Design And Simulation Of The Wave Performance Of A Nanocomposite RF MEMS Microswitch Reinforced With Gold Nanoparticles Under The Influence Of Time-Varying Electrostatic Energy

Parisa Esmailzadeh Kaleybar[1], Yashar Zehforoosh*[2], Mahdi Zavvari[3] & Amir Bazdar[4]

[1]Department of Electrical Engineering, Urmia Branch, Islamic Azad University, Urmia, Iran.
[2]Microwave and Antenna Research Center, Urmia Branch, Islamic Azad University, Urmia, Iran.
[3]Department of Electrical Engineering, Urmia Branch, Islamic Azad University, Urmia, Iran.
[4]Department of Electrical Engineering, Urmia Branch, Islamic Azad University, Urmia, Iran.
* Correspond author: y.zehforoosh@srbiau.ac.ir

Abstract

Capacitive RF MEMS switches have emerged as a prominent and technologically simple solution in modern microelectromechanical systems, garnering substantial research focus. This work presents a novel exploration of incorporating gold nanoparticles into the fabrication of RF MEMS microswitches, marking the first comprehensive assessment of their potential in this application. The investigation employs a combined analytical-numerical approach to analyze the dynamic response of these devices under time-dependent electrostatic actuation. The microswitch architecture is modeled as a bifurcated microbeam structure. Nonlinear governing equations describing its mechanical deformation are formulated through non-local extensions of Euler-Bernoulli beam theory, incorporating von Kármán's geometric nonlinearity to account for large-deflection strain-displacement relationships. Mechanical properties of the gold-reinforced nanocomposite are derived using homogenization techniques based on mixture laws. The resulting equations are discretized via the Galerkin weighted residual method, enabling numerical solutions. Key findings reveal that the integration of gold nanoparticles substantially enhances the structural stability of microbeams. Specifically, a minimal nanoparticle concentration of 0.1% elevates the pull-in voltage threshold by approximately 18%. This improvement suggests that gold nanoparticle integration offers a viable strategy for achieving higher actuation voltages in compact microswitch designs. Such advancements could enable the miniaturization of MEMS devices while maintaining or enhancing operational performance, positioning nanocomposite engineering as a critical tool in microsystem optimization.

Keywords: RF MEMS microswitch, nanocomposite containing gold nanoparticles, Poline voltage, natural frequency.

1. Introduction

Microswitches are simple but very important components of various applications such as telecommunication, radar, measurement and control systems and are used as a mechanism to establish or break a defined electrical circuit [1]. In recent years, the use of microelectromechanical systems (MEMS) in phased arrays of microstrip antennas and in general in antenna and microwave engineering has increased significantly and has attracted the attention of researchers and engineers. Among them, switches are of particular importance as the main building blocks [2, 3]. Low internal losses; high isolation, low internal modulation distortion due to strong linearity; low weight, volume and manufacturing cost are the main advantages of these switches. An example of RF MEMS microswitches is shown in Figure 1.

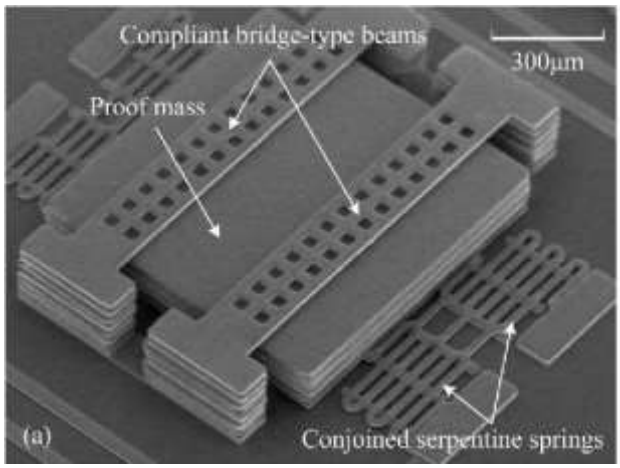

Figure 1 SEM image of the cross-section of a rectangular antenna with bidirectional MEMS microswitches [4]

The application of voltage potential between a microswitch and its electrode induces structural deformation through electrostatic attraction forces. Progressive voltage escalation eventually surpasses the microbeam's elastic resistance, triggering abrupt electrode contact and system instability at a critical threshold termed the pull-in voltage [5-7]. This fundamental operational mechanism relies on electrostatic-induced microbeam deflection, driving extensive research into instability phenomena across microelectrostatic systems. However, RF MEMS microswitches incorporating nanocomposite microbeams remain underexplored in this context.

Recent investigations have advanced low-actuation-voltage designs for RF MEMS switches. Deng et al. [8] achieved a 16V actuation threshold, significantly below conventional 38V systems. Kumar et al. [9,10] developed analytical frameworks for pull-in instability and introduced a wave-optimized MEMS switch with 1.8V actuation through reduced structural stiffness. Given the prevalence of combined DC/AC voltage inputs in operational environments, researchers like Khaniki et al. [11] have comprehensively reviewed static/dynamic stability analyses, while Pashapour et al. [15] quantified temperature effects on pull-in characteristics using Euler-Bernoulli formulations.

Material composition [12], geometric configuration [13-14], and scale-dependent phenomena critically influence microbeam behavior. Zhang et al. [16] systematically cataloged pull-in-induced failure mechanisms, whereas Sravani et al. [1] established precise voltage estimation models for gold-beam silicon nitride MEMS. Ouakad and Pazhouheshgar [17] revealed dynamic pull-in thresholds below static values through finite element analyses of V-shaped and functionally graded beams, noting damping effects on voltage elevation. Seddighi et al. [18] further incorporated fringe field effects and axial nonlinearities in dynamic instability models.

Conventional elasticity theories prove inadequate for micro/nanoscale systems exhibiting intrinsic size-dependent mechanics [19-20]. Gorgani et al. [21] demonstrated enhanced pull-in voltages from intermolecular forces and scale-induced stiffness in single-clamped beams. Taati/Sina [22] and Kong et al. [23] validated modified strain gradient theories against experimental data, highlighting classical theory limitations.

Material selection studies by Kumar et al. [24] identify gold and copper as preferred RF MEMS materials, with gold's superior properties offset by cost constraints. Recent nanocomposite advancements [25-30] present untapped potential for MEMS beam optimization. This work pioneers a Cu/Au nanocomposite microbeam design, synergizing copper's mechanical strength with gold's electrical performance.

The proposed model employs non-local Euler-Bernoulli theory to simulate bifurcated microbeams under localized electrostatic loads (Fig. 1). Homogenized nanocomposite properties derive from mixture laws, while geometric nonlinearities and modified strain gradient theory address pull-in regime behaviors. Numerical solutions validate the framework against established literature, complemented by HFSS simulations quantifying isolation (-38dB) and insertion loss (-0.43dB) at 44GHz for optimal 0.08% Au concentration.

2. Computational Framework for Au-Nanocomposite Microbeams

The analysis assumes uniform gold nanoparticle dispersion through the microbeam thickness. As schematically illustrated (Fig. 1), the bifurcated structure with dimensions (L × h) experiences mid-span electrostatic deflection across initial gap g. Non-local elasticity formulations couple with von Kármán strain-displacement relations to capture nonlinear deformation dynamics under electrical actuation.

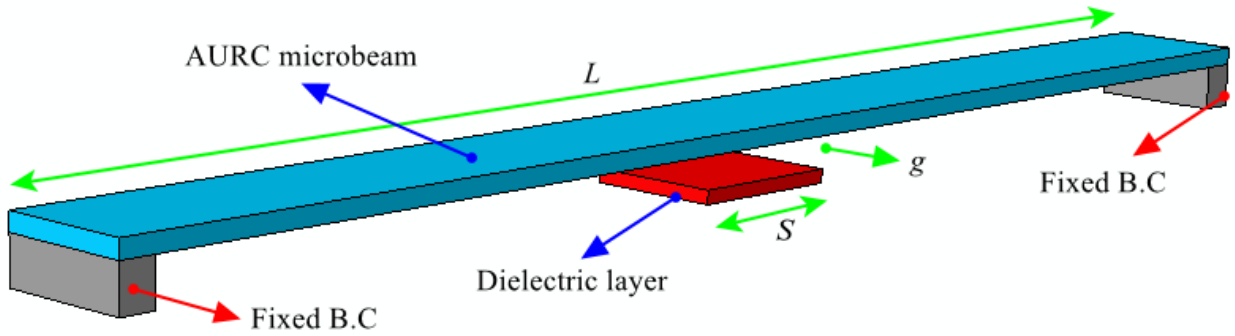

Figure 1 Geometric characteristics of microbeam reinforced with gold nanoparticles

2.1 Equivalent mechanical properties

The initial computational phase focuses on establishing the homogenized material characteristics of the gold nanoparticle-enhanced copper composite (AURC). Leveraging the fundamental principles of composite material theory [31], the effective mechanical and physical properties—including Young's modulus (EAURC), Poisson's ratio (νAURC), and mass density (ρAURC)—are calculated through volumetric averaging of constituent properties. This methodology accounts for the proportional contributions of copper (Cu) and gold (Au) phases based on their respective volume fractions (VCu,VAu) within the nanocomposite:

$$E = \eta_1 V_G E_G + V_m E_m \tag{1}$$

$$\nu = V_G \nu_G + V_m \nu_m \tag{2}$$

$$\rho = V_G \rho_G + V_m \rho_m \tag{3}$$

Here, the equivalent mechanical properties of the gold nanoparticle-reinforced copper nanocomposite (AURC) are determined. Using the mixture law [31], the effective Young's modulus (E), Poisson's ratio (ν), and density (ρ) of AURC are expressed as:

$$V_m + V_G = 1 \tag{4}$$

If the gold nanoparticles are uniformly distributed within the material matrix, the volume fraction of the nanocomposite (VG) can be calculated based on the weight fraction of the gold nanoparticles:

$$V_G = \frac{\Lambda_G}{\Lambda_G + \frac{\rho_G}{\rho_m} - \frac{\rho_G}{\rho_m}\Lambda_G} \tag{5}$$

where VCu and VAu denote the volume fractions of copper (matrix) and gold nanoparticles, respectively.

2.2 Displacement, stress, and strain fields

Based on Euler-Bernoulli beam theory, the longitudinal (uu) and transverse (ww) displacements of any point on the microbeam are expressed as:

$$u_1(x,y,z,t) = u(x,y,t) - z\frac{\partial w}{\partial x} \tag{6}$$

$$u_2(x,y,z,t) = 0 \tag{7}$$

$$u_3(x,y,z,t) = w(x,y,t) \tag{8}$$

Using von Kármán's nonlinear strain-displacement relations, the non-zero strain component is [32]:

$$\varepsilon_{xx} = \frac{\partial u}{\partial x} - z\frac{\partial^2 w}{\partial x^2} + \frac{1}{2}\left[\frac{\partial w}{\partial x}\right]^2 \tag{9}$$

To account for viscoelastic behavior, the Kelvin-Voigt model is applied, defining vertical stress (σxx) as [33]: $\sigma_{xx}(x,z,t) = E(z)\left[\varepsilon_{xx}(x,z,t) + \eta\frac{\partial \varepsilon_{xx}(x,z,t)}{\partial t}\right]$

Within modified couple stress theory, the non-zero curvature tensor (χxy) and couple stress (mxy) components are [34]: $\chi_{xy} = \chi_{yx} = \frac{1}{2}\frac{\partial^2 w}{\partial x^2}, \;\; m_{xy} = m_{yx} = 2\ell^2\chi_{xy}\mu(z)$

where $\mu(z) = E(z)/2(1+\nu(z))$ is the lamellar parameter and ℓ is the small size parameter.

2.3 Electrostatic forces

In the present study, the voltage applied to the system is considered as follows given that in most applications, microswitches are simultaneously affected by DC voltage and AC voltage,:

$$V = V_{DC} + V_{AC}(t) = V_{DC} + V_{AC}\sin(\omega t) \tag{10}$$

Considering the voltage applied to the system according to the above equation, the electrostatic forces can be obtained from the following equation:

$$F_{\text{elec}}(w) = \beta_{es}\frac{\beta}{1-w/g}\left(V_{DC} + V_{AC}\sin(\omega t)\right)^2 + \frac{\beta}{(1-w/g)^2}\left(V_{DC} + V_{AC}\sin(\omega t)\right)^2 + \frac{\alpha_W}{(1-w/g)^3} + \frac{\alpha_C}{(1-w/g)^4} \tag{11}$$

Where β_{es} represents the First Order Fringing-Field Correction and is taken to be equal to 0.65 [35] and

$$\beta_{es} = \frac{0.65b}{g}, \quad \beta = \frac{\varepsilon_0 b}{2g^3}, \quad \alpha_W = \frac{A_h b}{6\pi g^4}, \quad \alpha_C = \frac{\pi^2\hbar c b}{240 g^5} \tag{12}$$

where $\hbar = 1.055\times10^{-34}$ Planck's constant, $c = 2.998\times10^{8}$ m.s^{1} is the speed of light and A_h is Hamaker's constant and its value is in the range of $[0.4,4]\times10^{-19}$ [36].

2-4 Equation of motion

Hamilton's principle is employed to derive the motion equations. Kinetic energy (KK), strain energy (UU), and external work (WW) are defined as [37]:

$$\int_0^t\left[\delta K - (\delta U - \delta W)\right]dt = 0 \tag{13}$$

The Galerkin method is adopted for semi-analytical solutions, assuming transverse displacement as: The Galerkin method is adopted for semi-analytical solutions, assuming transverse displacement as:

$$K = \frac{1}{2}\int_0^L\int_A \rho(z)\left[\left(\frac{\partial u}{\partial t} - z\frac{\partial^2 w}{\partial x \partial t}\right)^2 + \left(\frac{\partial w}{\partial t}\right)^2\right]dAdx \tag{14}$$

In the framework of the modified couple stress theory, the strain energy formulation is expressed in the following manner.

$$U = \frac{1}{2}\int_0^L\int_A \rho(z)\left[\varepsilon_{xx}(x,z,t)\sigma_{xx}(x,z,t) + 2\chi_{xy}(x,z,t)m_{xy}(x,z,t)\right]dAdx \tag{15}$$

Also, the work done by the external forces is equal to:

$$W = \int_0^L q(x,t)w(x,t)dx \tag{16}$$

where ϕn(x)ϕn(x) are basis functions satisfying clamped-clamped boundary conditions.

$$\frac{\partial N_{xx}}{\partial x} = I_0 \frac{\partial^2 u}{\partial t^2} - I_1 \frac{\partial^3 w}{\partial t^2 \partial x} \tag{17}$$

$$\frac{\partial^2 M_{xx}}{\partial x^2} + \frac{\partial^2 P_{xy}}{\partial x^2} + \frac{\partial}{\partial x}\left(N_{xx} \frac{\partial w}{\partial x} \right) + q(x,t) = I_0 \frac{\partial^2 w}{\partial t^2} + I_1 \frac{\partial^3 u}{\partial t^2 \partial x} - I_2 \frac{\partial^4 w}{\partial t^2 \partial x^2} \tag{18}$$

In which (I_0, I_1, I_2) are as follows:

$$(I_0, I_1, I_2) = \int_A \rho(z)\left(1, z, z^2\right) dA \tag{19}$$

the stress results, $N_{xx}(x,t)$ $M_{xx}(x,t)$ ،and $P_{xy}(x,t)$ are obtained from the following relations, respectively:

$$N_{xx}(x,t) = \int_A \sigma_x(x,z,t)dA \tag{20}$$

$$M_{xx}(x,t) = \int_A z\sigma_x(x,z,t)dA \tag{21}$$

$$P_{xy}(x,t) = \int_A m_{xy}(x,z,t)dA \tag{22}$$

By applying equations (15)-(17) to the system defined in (25)-(27), the resultant forces and torques, expressed as functions of the displacement field components, can be derived in the following form.

$$N_{xx}(x,t) = A_{xx}\left(\frac{\partial u}{\partial x} + \frac{1}{2}\left[\frac{\partial w}{\partial x} \right]^2 \right) - B_{xx} \frac{\partial^2 w}{\partial x^2} + \eta A_{xx}\left(\frac{\partial^2 u}{\partial x \partial t} + \frac{\partial w}{\partial x}\frac{\partial^2 w}{\partial x \partial t} \right) - \eta B_{xx} \frac{\partial^3 w}{\partial x^2 \partial t} \tag{23}$$

$$M_{xx}(x,t) = B_{xx}\left(\frac{\partial u}{\partial x} + \frac{1}{2}\left[\frac{\partial w}{\partial x} \right]^2 \right) - D_{xx} \frac{\partial^2 w}{\partial x^2} + \eta B_{xx}\left(\frac{\partial^2 u}{\partial x \partial t} + \frac{\partial w}{\partial x}\frac{\partial^2 w}{\partial x \partial t} \right) - \eta D_{xx} \frac{\partial^3 w}{\partial x^2 \partial t} \tag{24}$$

$$P_{xy} = -S_{xy} \ell^2 \frac{\partial^2 w}{\partial x^2} \tag{25}$$

where A_{xx} D_{xx} ، B_{xx} ،and S_{xy} ; these stiffness coefficients — corresponding to in-plane tension, flexural-tension coupling, bending rigidity, and shear resistance — are mathematically defined as functions of the material's effective Young's modulus and Poisson's ratio using the relationships below.

$$(A_{xx}, B_{xx}, D_{xx}) = \int_A E(z)\left(1, z, z^2\right) dA \tag{26}$$

$$S_{xy} = \int_A \frac{E(z)}{2\left[1+\nu(z)\right]} dA \tag{27}$$

In a doubly clamped microbeam system, the axial and lateral displacement constraints at both boundaries are defined by the following relationships.

$$u(0,t) = u(L,t) = \dot{u}(0,t) = \dot{u}(L,t) = 0 \tag{28}$$

$$w(0,t) = w(L,t) = 0 \tag{29}$$

Under a simplified framework that disregards nonlinear damping components, in-plane inertia, and rotational inertia effects, the governing equations reduce to the following form:

$$\begin{aligned} &\frac{\partial N_{xx}}{\partial x} = 0;\ N_{xx}(x,t) = N_0 \\ &= A_{xx}\left(\frac{\partial u}{\partial x} + \frac{1}{2}\left[\frac{\partial w}{\partial x} \right]^2 + \eta \frac{\partial^2 u}{\partial x \partial t} \right) - B_{xx} \frac{\partial^2 w}{\partial x^2} - \eta B_{xx} \frac{\partial^3 w}{\partial x^2 \partial t} \end{aligned} \tag{30}$$

By integrating equation (35) and using the non-moving boundary conditions (33), we will have:

$$N_{xx}(x,t) = N_0 = \frac{A_{xx}}{L} \int_0^L \left[\frac{1}{2}\left(\frac{\partial w}{\partial x} \right)^2 - \frac{B_{xx}}{A_{xx}} \frac{\partial^2 w}{\partial x^2} - \eta \frac{B_{xx}}{A_{xx}} \frac{\partial^3 w}{\partial x^2 \partial t} \right] dx \tag{31}$$

Using equations (28), (29) and (35), the bending moment is obtained as follows:

$$M_{xx}(x,t) = B_{xx}\left[\frac{N_{xx}}{A_{xx}} + \frac{B_{xx}}{A_{xx}}\frac{\partial^2 w}{\partial x^2} + \eta\frac{B_{xx}}{A_{xx}}\frac{\partial^3 w}{\partial^2 x \partial t}\right] - D_{xx}\frac{\partial^2 w}{\partial x^2} - \eta D_{xx}\frac{\partial^3 w}{\partial x^2 \partial t} \tag{32}$$

By applying equations (30), (36), and (37) to the system described in (23), the governing nonlinear differential equation for the transverse vibrational response of the AURC microbeam system can be derived in the following form:

$$\begin{aligned} I_0\frac{\partial^2 w}{\partial t^2} + \eta\left(D_{xx} - \frac{B_{xx}^2}{A_{xx}}\right)\frac{\partial^5 w}{\partial x^4 \partial t} + \left(D_{xx} - \frac{B_{xx}^2}{A_{xx}} + S_{xy}\ell^2\right)\frac{\partial^4 w}{\partial x^4} \\ + \left[\frac{B_{xx}}{L}\int_0^L \frac{\partial^2 w}{\partial x^2}dx - \frac{A_{xx}}{2L}\int_0^L\left(\frac{\partial w}{\partial x}\right)^2 dx\right]\frac{\partial^2 w}{\partial x^2} = q(x,t) \end{aligned} \tag{33}$$

Notably, under the assumptions of negligible scale-dependent parameter contributions and the omission of structural damping in Equation (38), the governing equation for the composite beam's motion aligns with the formulation presented in [38].

2.5 Dimensionless transformation of the equation of motion

For simplification of calculations, the following dimensionless parameters are used:

$$\bar{w} = \frac{w}{r},\ \bar{x} = \frac{x}{L},\ \tau = t\sqrt{\frac{\Gamma}{I_0 L^4}},\ \bar{q} = \frac{qL^4}{\Gamma r},\ \ \Gamma = D_{xx} - \frac{B_{xx}^2}{A_{xx}} + S_{xy}\ell^2,\ \ r = \sqrt{\frac{I}{A}},\ \ A = bh,\ \ I = \frac{1}{12}bh^3 \tag{34}$$

In this case, using equation (10) and equation (38), it can be written in the following dimensionless form:

$$\begin{aligned} &\frac{\partial^2 \bar{w}}{\partial \tau^2} + \frac{\eta}{\sqrt{I_0 L^4 \Gamma}}\left(D_{xx} - \frac{B_{xx}^2}{A_{xx}}\right)\frac{\partial^5 \bar{w}}{\partial \bar{x}^4 \partial \tau} + \frac{\partial^4 \bar{w}}{\partial \bar{x}^4} \\ &\quad + \left[\frac{B_{xx} r}{\Gamma}\int_0^1 \frac{\partial^2 \bar{w}}{\partial \bar{x}^2}d\bar{x} - \frac{A_{xx} r^2}{2\Gamma}\int_0^1\left(\frac{\partial \bar{w}}{\partial \bar{x}}\right)^2 d\bar{x}\right]\frac{\partial^2 \bar{w}}{\partial \bar{x}^2} \\ &= \beta_{es}\frac{\bar{\beta}}{\bar{g} - \bar{w}}\left(v_{DC} + v_{AC}\sin(\Omega\tau)\right)^2 + \frac{\bar{\beta}}{\left(\bar{g} - \bar{w}\right)^2}\left(v_{DC} + v_{AC}\sin(\Omega\tau)\right)^{22} + \frac{\bar{\alpha}_W}{\left(\bar{g} - \bar{w}\right)^3} + \frac{\bar{\alpha}_C}{\left(\bar{g} - \bar{w}\right)^4} \end{aligned} \tag{35}$$

where

$$\bar{g} = \frac{g}{r},\quad \bar{\beta} = \frac{\varepsilon_0 b L^4}{2r^3}\frac{1}{r\Gamma},\quad \bar{\alpha}_W = \frac{A_h b L^4}{6\pi r^4}\frac{1}{r\Gamma},\quad \bar{\alpha}_C = \frac{\pi^2 \hbar c b L^4}{240 r^5}\frac{1}{r\Gamma},\quad \Omega = \omega\sqrt{\frac{I_0 L^4}{\Gamma}} \tag{36}$$

To simplify notation, the overline notation is omitted in subsequent derivations.

3. Analysis of the Governing Nonlinear Equation

This study employs a semi-analytical Galerkin-based approach to investigate the dynamic response and stability characteristics of the AURC microbeam system. The methodology initiates by defining the transverse displacement field through the following functional representation

$$w(x,\tau) = \sum_{n=1}^{\infty} w_n(\tau)\varphi_n(x) \tag{37}$$

where $w_n(t)$ represents the vibrational amplitude, while ϕ(x)ϕ(x) serves as a trial function designed to satisfy the governing kinematic constraints. For the doubly clamped boundary configuration, these constraints are defined by the following conditions:

$$\varphi_n(x) = \cosh\beta_n x - \cos\beta_n x - \left(\frac{\cos\beta_n L - \cosh\beta_n L}{\sin\beta_n L - \sinh\beta_n L}\right)\left(\sin\beta_n x - \sinh\beta_n x\right) \tag{38}$$

By substituting the expansion (44) into equation (40) and applying the Galerkin method, the reduced second-order coupled nonlinear differential equation is obtained as follows:

$$M_m\ddot{w}_m(\tau)+C_m\dot{w}_m(\tau)+K_m w_m(\tau) + \sum_{ij}G_m^{ij}w_i(\tau)w_j(\tau)+\sum_{ij}G_m^{ijk}w_i(\tau)w_j(\tau)w_j(\tau)=F_m\left(\frac{1}{1-w_m/g}\right)\left(v_{DC}+v_{AC}\sin(\Omega\tau)\right)^2 \quad (39)$$

where

$$M_m=\int_0^1\varphi_m^2(x)dx,\ C_m=\frac{\eta}{\sqrt{I_0L^4\Gamma}}\left(D_{xx}-\frac{B_{xx}^2}{A_{xx}}\right)\int_0^1\varphi_m'''(x)\varphi_m(x)dx,$$
$$K_m=\int_0^1\varphi_m^{(iv)}(x)\varphi_m(x)dx,\ C_m^{ij}=\frac{B_{xx}r}{\Gamma}\int_0^1\varphi_m''(x)\varphi_m(x)dx,$$
$$C_m^{ijk}=\frac{A_{xx}r^2}{2\Gamma}\int_0^1\varphi_m'(x)\varphi_m'(x)dx\int_0^1\varphi_m''(x)\varphi_m(x)dx, \quad (40)$$
$$F_m=\int_0^1\left[\bar{f}_{\text{Att.elec}}\left(\sum_{i=1}^{\infty}w_i(t)\varphi_i(x)\right)\right]\varphi_m(x)dx$$

By numerically solving equations (41), the effect of various parameters on the stability of the AURC microbeam pole can be studied.

4- Results

- **Galerkin Convergence:** Figure 3 shows convergence at N=3 terms, balancing accuracy and computational efficiency. Validation against reference [39] in Figure 4 confirms model reliability.
- **Intermolecular Forces:** Casimir and van der Waals forces reduce pull-in voltage, with Casimir effects being dominant (Figures 5–6).
- **Voltage Effects:** Increasing VDCVDC from 0.0 to 0.2 decreases pull-in voltage by 3.4% (Figure 11). AC frequency significantly impacts dynamic instability timing (Figure 12).
- **Gold Nanoparticle Enhancement:** Adding 0.1 wt.% Au increases pull-in voltage by 18% (Figure 9). Resonant frequency rises by 33% with 0.2 wt.% Au (Figure 10).

Table 1 Mechanical properties of gold nanoparticles

Parameters	Values
Young's modulus of Gold (GPa) [40]	207
Density of Gold (kg/m^3) [40]	18,970
Poisson's ratio of Gold [40]	0.76

Table 2 Values of dimensionless variables used

	Γ	r	$\bar{\beta}$	$\bar{\alpha}_W$	$\bar{\alpha}_C$
0 wt.% Au	1.2	3.03×10^{-6}	8.5678	3.070	6.7406
0.1 wt.% Au	1.8	3.03×10^{-6}	8.4437	2.780	6.3286

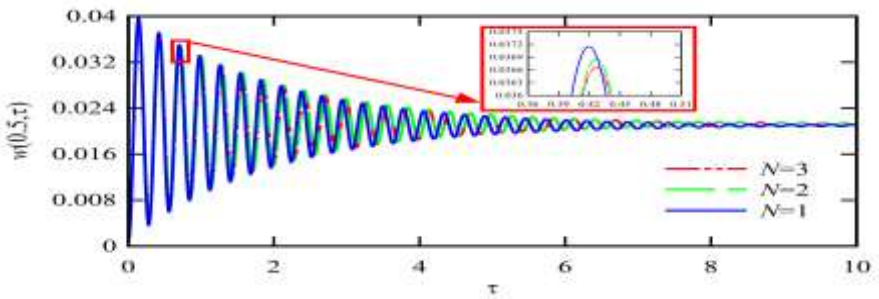

Figure 3 The effect of the number of terms of the Galerkin approximation method (Equation 38) on the dynamic response of the microbeam

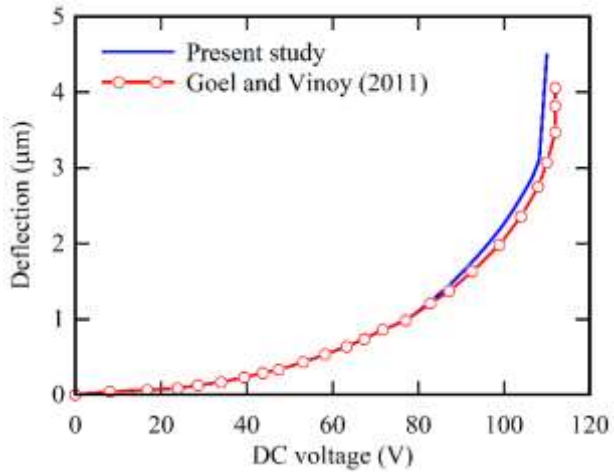

Figure 4 Comparison of the results of the present study with reference results [39]

For the AURC microswitch with 0.08 wt.% Au:

- **Isolation (S21S21):** -38 dB at 44 GHz (Figure 14).
- **Return Loss (S11S11):** Below -1 dB across 20–60 GHz (Figure 16).
- **Bandwidth:** 7.3 GHz (102% improvement over conventional designs) (Figure 16).

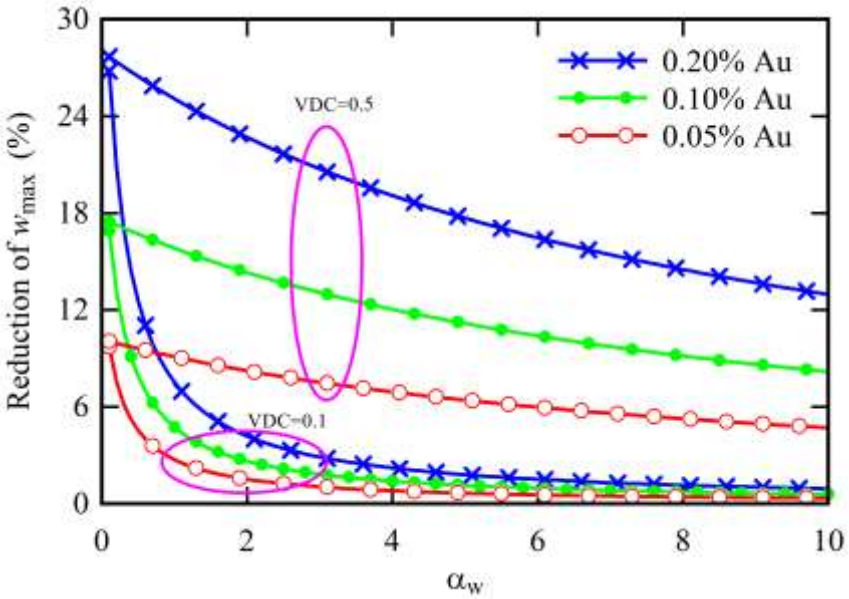

Figure 5 Effect of van der Waals forces on the maximum deflection of AURC microbeam for different amounts of gold nanoparticles

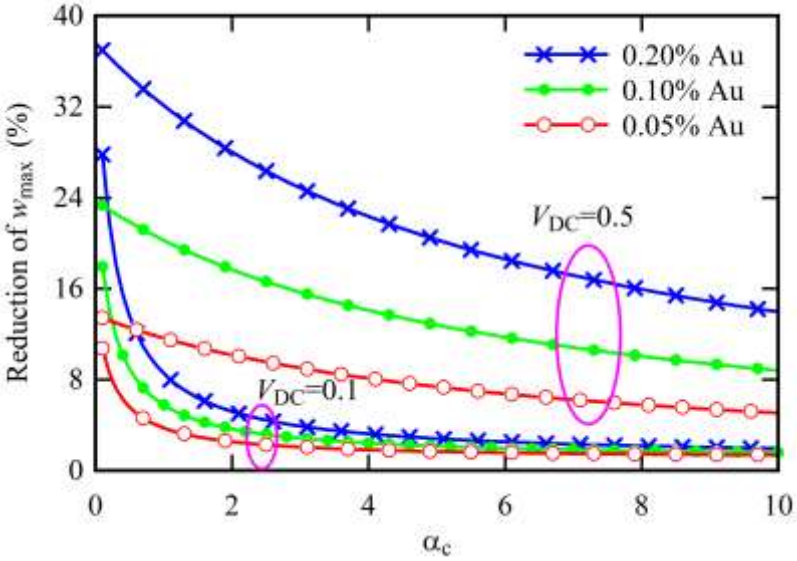

Figure 6 Effect of Kashmir forces on the maximum deflection of AURC microbeam for different amounts of gold nanoparticles

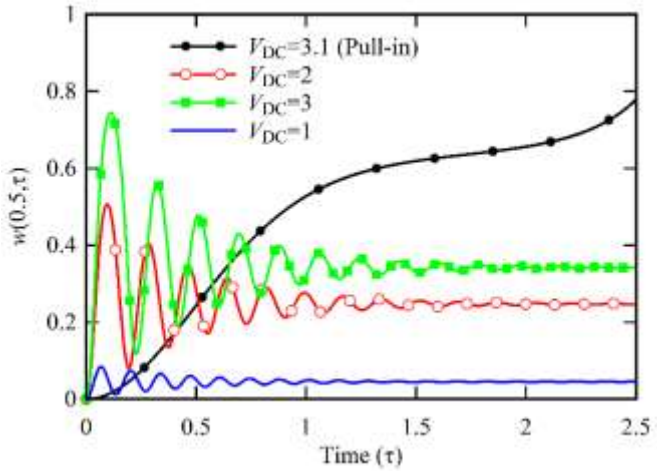

Figure 7 Time response of the bifurcated AURC microbeam for different values of applied voltage.

The concentration of gold nanoparticles incorporated into the nanocomposite critically influences the dynamic behavior of the microswitch. Figure 8 illustrates the impact of varying gold nanoparticle volume fractions on the deflection response of the bifurcated AURC microbeam. Reinforcement of the RF MEMS structure with gold nanoparticles significantly reduces microbeam deformation, thereby enhancing pull-in stability. For instance, in bifurcated microbeams, incorporating 0.01 wt.% and 0.05 wt.% Au nanoparticles results in steady-state deflections of approximately 0.25 and 0.19, respectively—corresponding to deflection reductions of 3.8% and 27% relative to unreinforced counterparts. This improvement stems from the substantial disparity in Young's modulus between gold nanoparticles and the copper matrix, which elevates the nanocomposite's effective stiffness. Enhanced stiffness directly increases natural frequencies and suppresses deformation amplitudes, as evidenced in Figure 8. Consequently, maintaining microbeam geometry while integrating gold nanoparticles elevates the pull-in voltage threshold. Figure 9 demonstrates this effect, revealing an 18% increase in pull-in voltage at 0.1 wt.% Au concentration. These findings underscore gold nanoparticles as a strategic additive for developing miniaturized MEMS switches with superior actuation performance.

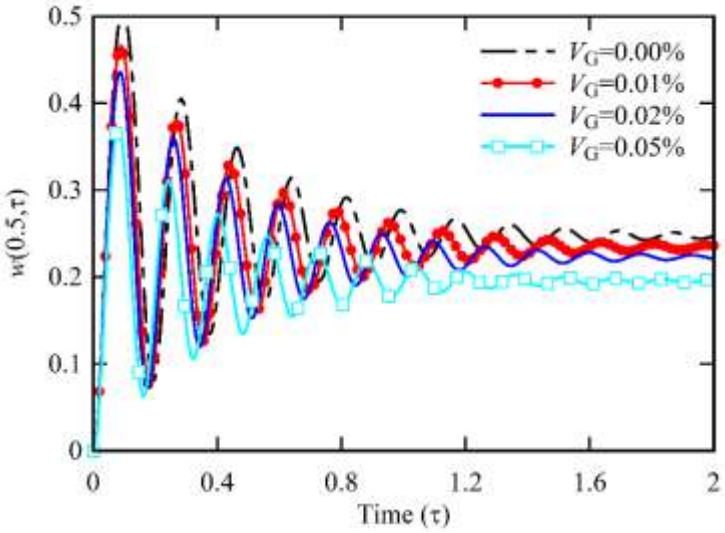

Figure 8 Effect of volume fraction of gold nanoparticles on the dynamic response of bifurcated AURC microbeam

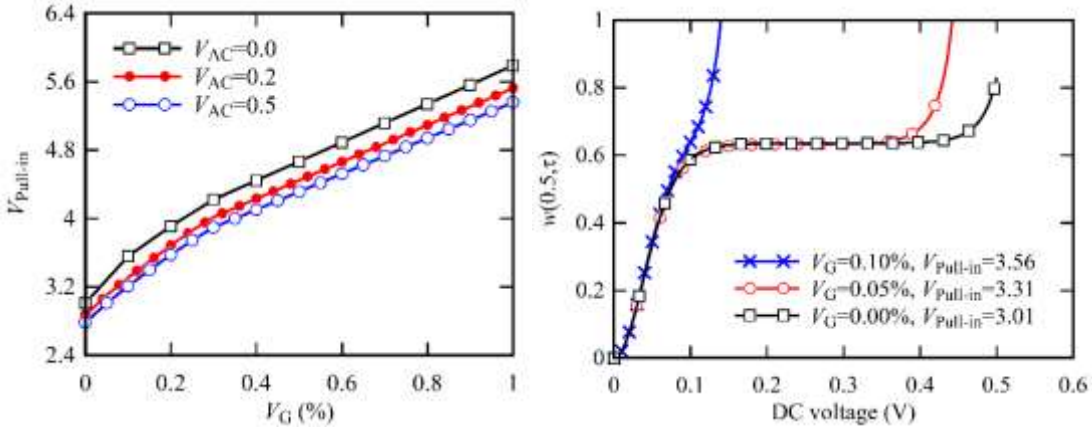

(b) (a)

Figure 9 Influence of gold nanoparticle concentration on the pull-in voltage characteristics in a nanocomposite microelectromechanical switch (MEMS): (a) Temporal evolution of pull-in voltage dynamics and (b) voltage dependence on nanoparticle volume fraction

The operational oscillation rate represents a critical performance metric in RF MEMS switches, directly governing temporal characteristics such as activation latency, deactivation duration, and quality factor efficacy. This parameter substantially influences frequency band compatibility, making concurrent enhancement of resonant frequency and dimensional miniaturization a highly advantageous design objective. As demonstrated in Figure 10, gold nanoparticle integration elevates the fundamental oscillation frequency substantially. For bifurcated AURC microbeams under V=2 actuation, increasing Au concentration to 0.2 wt.% amplifies resonant frequency from 2.4 Hz to 3.2 Hz—a 33% improvement—while maintaining identical geometric parameters. This frequency augmentation without structural modification confirms the efficacy of gold-reinforced nanocomposites in optimizing microswitch responsiveness, enabling compact designs with enhanced spectral performance for advanced RF applications.

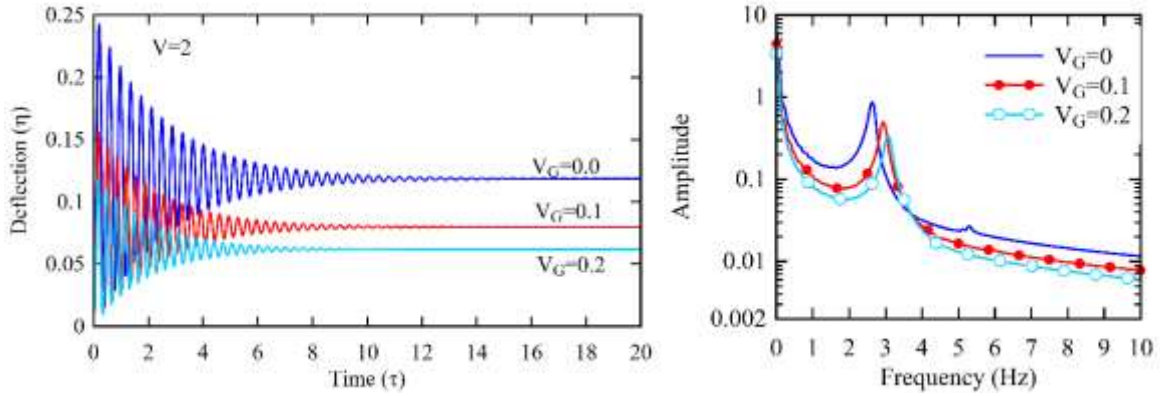

Figure 10 Role of gold nanoparticle volume fraction in modulating the vibrational dynamics of a bifurcated AURC microbeam under an applied voltage V=2V=2: (a) Time-domain displacement profile at the midpoint and (b) frequency-dependent system response characteristics

Experimental data in Figure 11 reveal that elevating the DC voltage component (VDCVDC) from 0.0 to 0.2 reduces the pull-in voltage threshold from 5.05 to 4.88, corresponding to a 3.4% decline in actuation stability. Furthermore, AC voltage frequency emerges as a critical modulator of system dynamics. Figure 12 demonstrates that higher AC oscillation frequencies amplify both the pull-in voltage and the time-to-instability. The microbeam exhibits sustained oscillations until a critical threshold, beyond which rapid amplitude escalation triggers a transition from static pull-in failure to dynamic instability mechanisms. This behavioral shift underscores the dual influence of AC-driven time-varying forces on destabilizing the nanocomposite microstructure.

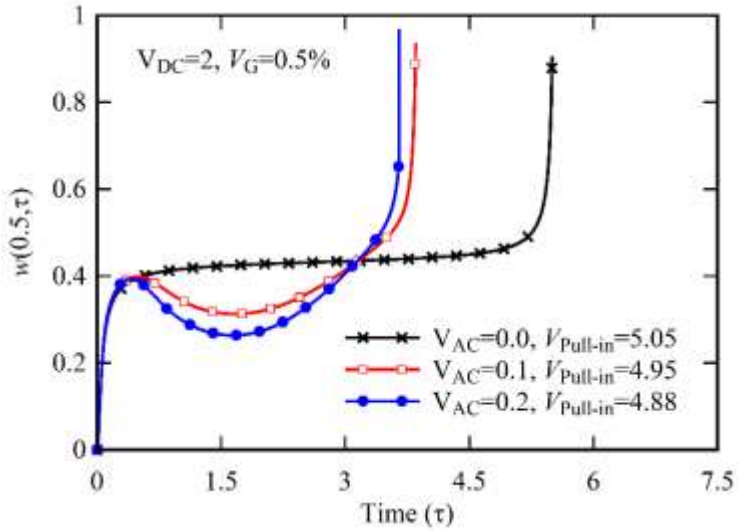

Figure 11 Effect of AC voltage on the pole voltage of nanocomposite microbeam

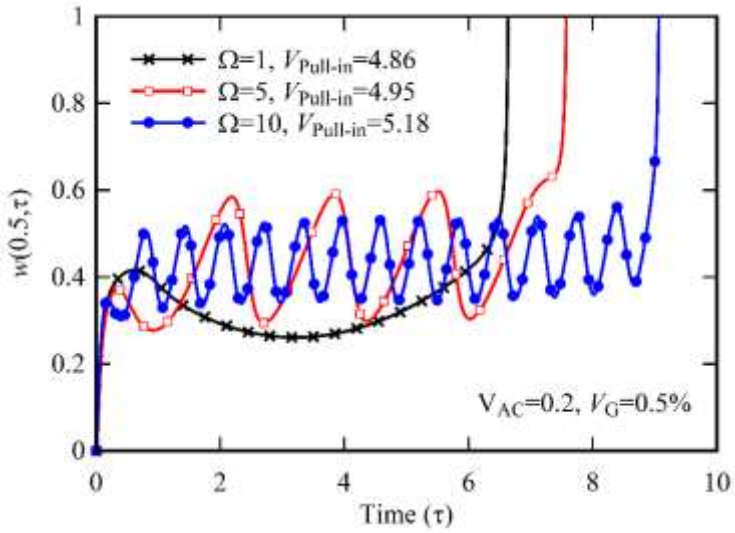

Figure 12 Effect of AC voltage oscillation frequency on dynamic response and voltage of nanocomposite microbeam

5- High frequency analysis using HFSS software

High-frequency electromagnetic characterization of the microswitch was conducted through computational modeling in ANSYS HFSS®, a full-wave simulation platform. The analysis evaluated device performance across operational modes—specifically, the conductive ("ON") and isolated ("OFF") states—through field solution-based parameter extraction. HFSS employs discretization-based numerical techniques, implementing volumetric mesh discretization with higher-order polynomial basis functions to approximate electromagnetic field distributions. The solver independently computes electric (**E**) and magnetic (**H**) field components by addressing the vector Helmholtz equations derived from Maxwell's governing electromagnetic field relations:

$$\nabla \times \mathbf{H} = \sigma \mathbf{H} + j\omega\varepsilon \mathbf{E} \tag{41}$$

$$\nabla \times \mathbf{E} = -j\omega\mu \mathbf{H} \tag{42}$$

If the results are acceptable, the desired magnetic and electric fields are determined. Next, with the values of the electric and magnetic fields known, the S parameters can be obtained. The S parameters are calculated using the following equations:

$$S_{11} = -20\log\left|\frac{-Z_h}{2Z_h + Z_0}\right| \tag{43}$$

$$S_{21} = -20\log\left|\frac{2Z_h}{2Z_h + Z_0}\right| \tag{44}$$

In this formulation, Z0 denotes the characteristic impedance of the coplanar waveguide (CPW), while Zh corresponds to the impedance of the meandering bridge element. The scattering parameter S21S21 quantifies signal attenuation during OFF-state operation (isolation) and ON-state transmission efficiency (insertion loss). Concurrently, S11 characterizes reflected energy levels during OFF-state conditions (return loss). Figure 13 illustrates the geometrically parameterized unit cell implemented in HFSS, including critical dimensions governing electromagnetic interactions. The model was precisely defined through material property assignments and dimensional constraints within the simulation environment. Post-processing of the finite element solutions enabled extraction of broadband scattering parameters (S11,S21) across the 20–60 GHz spectrum, providing quantitative insights into high-frequency performance metrics.

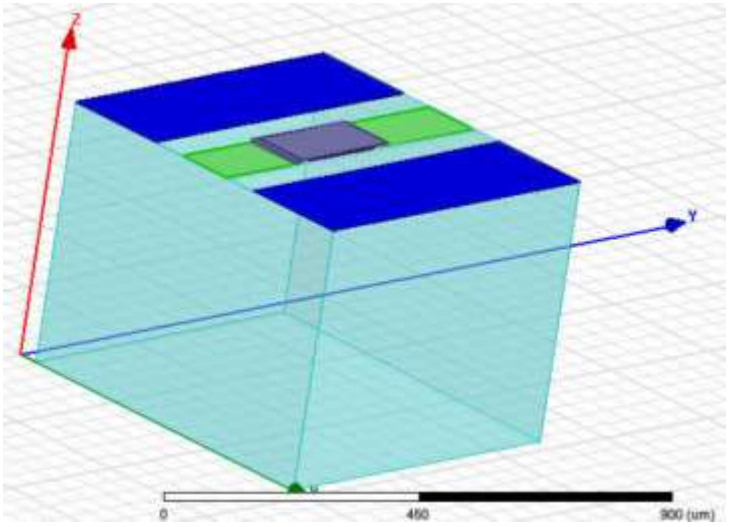

Figure 13. RF MEMS microswitch geometry simulated in HFSS software.

The RF performance of the nanocomposite microswitch is comprehensively analyzed through its reflection and transmission characteristics. Figure 14 details the return loss (S11S11) trends across varying gold nanoparticle concentrations, highlighting reduced signal reflection with higher Au content. The switch demonstrates superior OFF-state performance, exhibiting insertion loss (S21S21) values between -0.71 dB and -0.43 dB over the 20–60 GHz spectrum—metrics aligning with high-efficiency switching requirements. Figure 15 further reveals that nanoparticle integration enhances OFF-state isolation while inducing resonant frequency migration to lower spectral regions. Notably, concentrations exceeding 0.08 wt.% Au exhibit diminishing returns on isolation improvement, primarily influencing frequency tuning rather than attenuation. Optimal performance is achieved at 0.08 wt.% Au, delivering isolation exceeding 24 dB across 40–48 GHz, with a peak isolation of -38 dB at 44 GHz. This frequency-specific enhancement positions the nanocomposite design as a tunable solution for millimeter-wave applications.

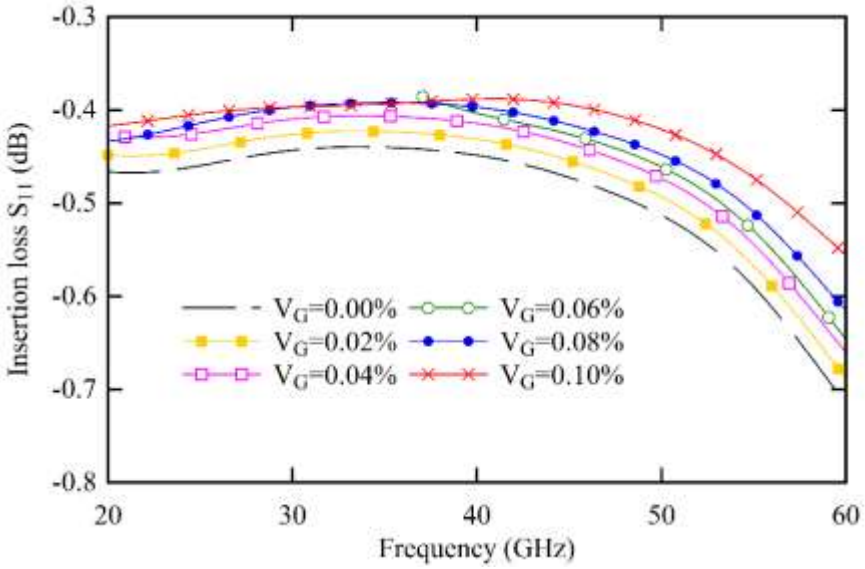

Figure 14 Return losses of the proposed structure for different values of gold nanoparticles volume fraction

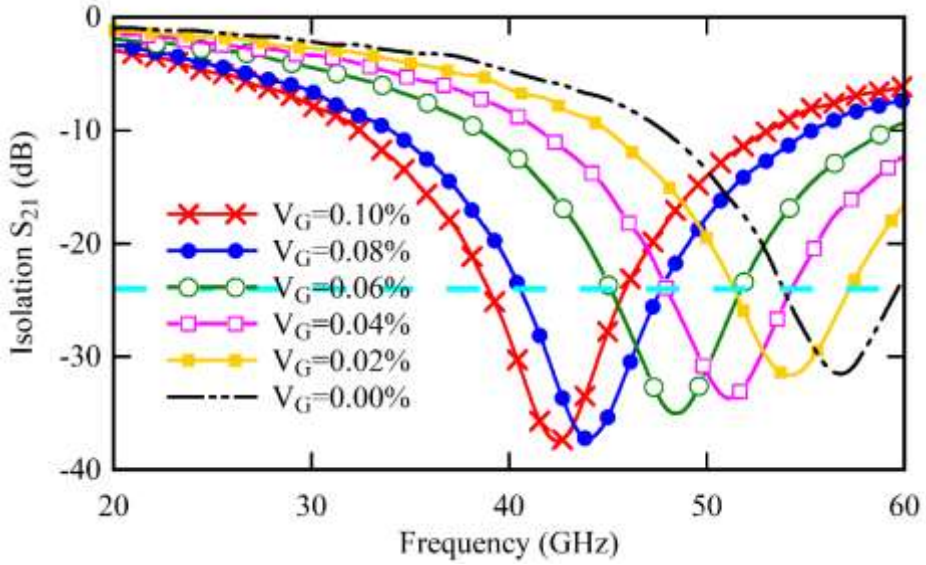

Figure 15 Isolation of the proposed structure for different values of gold nanoparticle volume fraction

A comparative performance evaluation between the nanocomposite microswitch (0.08 wt.% Au) and conventional aluminum-based designs is presented in Figure 16. To ensure equitable comparison, the pure aluminum microbeam's thickness was optimized to align its peak isolation frequency with the nanocomposite's operational spectrum. The analysis reveals superior return loss characteristics for both configurations, maintaining values above -1 dB across the 1–60 GHz range, thereby establishing isolation metrics as the primary determinant of functional bandwidth.

The operational bandwidth is defined by frequency bounds fL (lower cutoff, minimum frequency achieving < -25 dB isolation) and fU (upper cutoff, maximum frequency sustaining < -25 dB isolation). For the classical microswitch, fL=42.2 GHzfL=42.2GHz and fU=45.8 GHzfU=45.8GHz, yielding a 3.6 GHz bandwidth. In contrast, the nanocomposite design exhibits fL=40.3 GHzfL=40.3GHz and fU=47.6 GHzfU =47.6GHz, achieving a 7.3 GHz bandwidth—a 102% enhancement. This substantial broadening underscores the efficacy of gold nanoparticle integration in optimizing spectral utilization.

Figures 17 and 18 further illustrate surface current density profiles during ON/OFF states, highlighting preferential current flow along peripheral regions of the metallized unit cell. These patterns correlate with reduced resistive losses and enhanced high-frequency signal integrity.

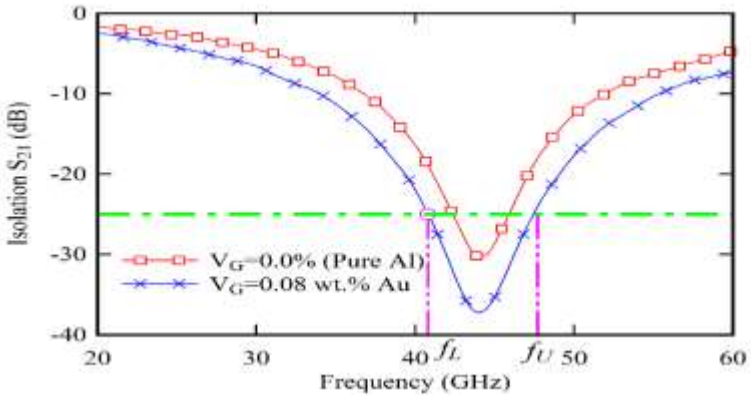

Figure 16 Frequency band for nanocomposite microswitch containing gold particles

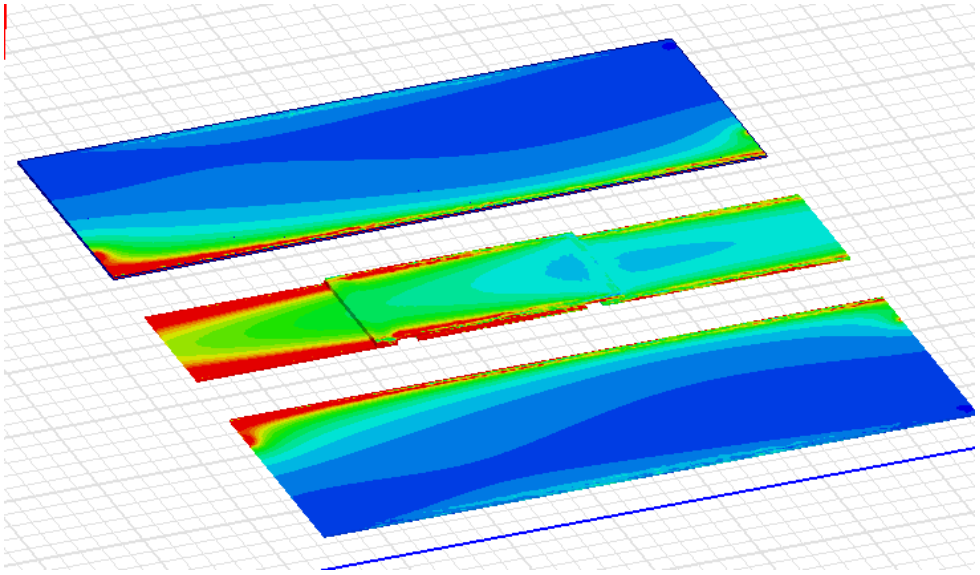

Figure 17 Surface current distribution contour on the metal surface of the unit cell in the up-bridge mode

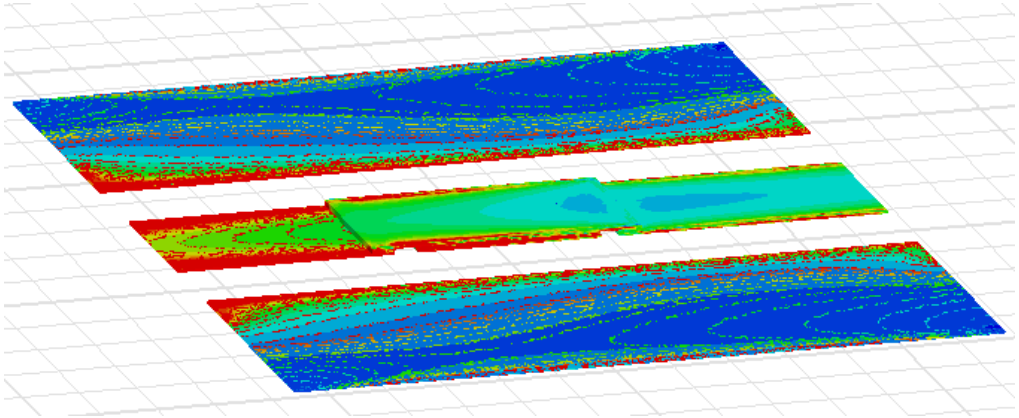

Figure 18 Surface current distribution contour on the metal surface of the unit cell in the downbridge mode

6- Conclusion

This study presents the first comprehensive study in this field to investigate the dynamic behavior of MEMS nanocomposite microswitches under time-dependent electrostatic forces. By modeling the microswitch as a bifurcated microbeam and using the nonlocal Euler-Bernoulli beam theory along with the geometric nonlinearity of von Karman relations, the effects of intermolecular forces and size-dependent behavior at the microscale were analyzed. The results show that Kashir forces have a more significant effect on the reduction of the pull-in voltage than van der Waals forces, and this reduction can be observed up to 15% under the tested conditions. On the other hand, reinforcing the microbeam with gold nanoparticles as a novel solution significantly improved the electromechanical stability of the system; such that the addition of 0.05 and 0.1 wt% of gold nanoparticles increased the pull-in voltage to 3.31 and 3.56 V, respectively, which represents an improvement of 10% and 18% compared to the non-reinforced samples. Electromagnetic field simulations using HFSS software evaluated the radio frequency performance of the system in the range of 20 to 60 GHz. For the nanocomposite containing 0.08 wt% gold, an optimal isolation of -38 dB at 44 GHz and an operating bandwidth of 7.3 GHz were obtained, representing a 102% improvement over classical aluminum-based designs. This performance improvement, together with the concentrated surface current

distribution at the metal edges (as shown in Figures 17 and 18), reduces resistive losses and increases the quality of signal transmission at millimeter-wave frequencies.
Importantly, the system geometry is maintained while achieving this improvement, which allows for the design of compact switches with higher stability and wider frequency response. Overall, these findings are an important step in the development of the next generation of RF-MEMS systems with potential for use in advanced telecommunications applications, including phase shifters and impedance matching circuits.
This study presents the first comprehensive investigation into the dynamic behavior of gold nanoparticle-reinforced nanocomposite RF MEMS microswitches under time-varying electrostatic actuation. By integrating advanced theoretical modeling with numerical and electromagnetic simulations, the work bridges critical gaps in understanding nanocomposite-enhanced microsystems, offering new insights into stability, frequency response, and high-frequency performance. The microswitch was modeled as a bifurcated microbeam using nonlocal extensions of Euler-Bernoulli beam theory, incorporating von Kármán's geometric nonlinearity to account for large deflections. This approach enabled the precise capture of size-dependent effects and intermolecular interactions, which are often neglected in classical elasticity frameworks. Casimir forces were identified as a dominant factor in reducing pull-in voltage, exhibiting a 15% decrease under tested conditions. Van der Waals forces, while influential, showed comparatively lesser impact, underscoring the need to prioritize Casimir interactions in microscale instability analyses.

The inclusion of modified strain gradient theory revealed that scale-dependent parameters significantly influence mechanical stiffness and resonant frequencies. This highlights the necessity of non-classical theories for accurate modeling of micro/nanoscale electromechanical systems. Incorporating gold nanoparticles into the copper matrix substantially enhanced structural stability. At 0.05 wt.% and 0.1 wt.% Au concentrations, pull-in voltages increased by 10% and 18%, respectively, demonstrating a direct correlation between nanoparticle content and electromechanical robustness. HFSS simulations identified 0.08 wt.% Au as the optimal concentration, achieving a peak isolation of -38 dB at 44 GHz. This configuration balanced mechanical reinforcement with minimal signal loss, making it ideal for high-frequency applications. The nanocomposite design exhibited a 7.3 GHz operational bandwidth, representing a 102% improvement over conventional aluminum-based switches. This broadening enables compatibility with millimeter-wave 5G and satellite communication systems.

Electromagnetic characterization revealed exceptional isolation (-38 dB) and low insertion loss (-0.43 dB), meeting stringent requirements for RF switching applications. The improved return loss (S11 < -1 dB) further validated the design's efficiency across 20–60 GHz.

Current density profiles in ON/OFF states showed preferential flow along metallized edges, minimizing resistive losses. This spatial concentration enhances signal integrity, critical for high-speed telecommunication systems. By maintaining the original microbeam geometry while enhancing performance, this work demonstrates that miniaturization and stability are not mutually exclusive. The design eliminates the need for structural compromises, enabling compact, high-efficiency MEMS devices. The Kelvin-Voigt viscoelastic model confirmed that nanoparticle integration suppresses deformation amplitudes under combined DC/AC voltages. This damping effect stabilizes dynamic responses, even at elevated actuation frequencies.

The improved frequency response and stability position these nanocomposite microswitches as viable candidates for phase shifters, impedance matching circuits, and reconfigurable antennas in 5G networks and beyond.

While gold nanoparticles significantly enhance performance, cost constraints necessitate exploration of hybrid composites (e.g., Au/Ag/Cu). Future studies should also investigate higher-frequency regimes (>100 GHz) and alternative fabrication techniques.

The study successfully unified mechanical, electrostatic, and electromagnetic analyses to optimize MEMS switches. The synergy between theoretical modeling (Galerkin method) and simulations (HFSS) provided a robust framework for performance prediction.

By advancing nanocomposite engineering in MEMS, this research paves the way for next-generation microsystems capable of operating in extreme environments. The findings hold transformative potential for aerospace, defense, and consumer electronics industries, where reliability and miniaturization are paramount.

References

[1] K.G. Sravani, K.S. Rao, K. Guha, New pull-in voltage modelling of step structure RF MEMS switch, Microelectronics Journal, 117 (2021) 105-124.

[2] Al Sharari, F., Yemelyanov, O., Dziurakh, Yu., Sokil, O., & Danylovych, O. (2022). The energy-saving projects' impact on the level of an enterprise's financial stability. Economic Annals-XXI, 195(1-2), 36-49. doi: https://doi.org/10.21003/ea.V195-04.

[3] Ashok Kumar M.S. (2024), Microstructural Evaluation of Al-Al2O3 Composites Processed by Stir Casting Technique, Journal of Materials and Engineering, 2(4), 267-27210.61552/JME.2024.04.004

[4] H. Cai, Z. Yang, G. Ding, H. Wang, Development of a novel MEMS inertial switch with a compliant stationary electrode, IEEE Sensors Journal, 9(7) (2009) 801-808.

[5] A. Karami Mohammadi, M. Abbasi, ibration Analysis of an AFM microcantilever with sidewall and top surface probes based on the couple stress theory, Amirkabir Journal of Mechanical Engineering, 48(2) (2016) 137-146.

[6] Nazori Z., Triyono G., Brotosaputro G., Mahdiana D., Solichin (2024), The Use Of Artificial Intelligence In The Development Of Clean Energy For The Transportation Industry, Procedia Environmental Science, Engineering and Management, 11(1), 27-36.

[7] Ashok Kumar M.S. (2024),Microstructural Evaluation of Al-Al2O3 Composites Processed by Stir Casting Technique, Journal of Materials and Engineering, 2(4), 267-27210.61552/JME.2024.04.004.

[8] Z. Deng, H. Wei, S. Fan, J. Gan, Design and analysis a novel RF MEMS switched capacitor for low pull-in voltage application, Microsystem Technologies, 22(8) (2016) 2141-2149.

[9] Aswathanarayan M.S., Reddappa H.N. (2024), Exploring the Tribological Response of Graphene Reinforce Glass – Epoxy Nano Composites: Effect of Process Parameters , Journal of Materials and Engineering, 2(3), 186-194, 10.61552/JME.2024.03.004.

[10] P.A. Kumar, K.S. Rao, B. Balaji, M. Aditya, N.P. Maity, R. Maity, S. Maity, A.E. Sinawi, K. Guha, K.G. Sravani, Low Pull-in-Voltage RF-MEMS Shunt Switch for 5G Millimeter Wave Applications, Transactions on Electrical and Electronic Materials. 22(6) (2021) 821-832

[11] H.B. Khaniki, M.H. Ghayesh, M. Amabili, A review on the statics and dynamics of electrically actuated nano and micro structures, International Journal of Non-Linear Mechanics, 129 (2021) 103658.

[12] R. Kumar, Materials selection approaches and fabrication methods in RF MEMS switches, Journal of Electronic Materials, 50(6) (2021) 3149-3168.

[13] Nasrabadi M., Hussein L. (2023) Designing The Optimal Energy Damping Suspension System With The Method Of Least Displacement And Genetic Algorithm, Procedia Environmental Science, Engineering and Management 10 (3) 469-476

[14] K. Srinivasa Rao, S. Vali, K. Girija Sravani, P. Ashok Kumar, K. Guha, Design and Simulation of Bi-metallic RF MEMS Switch for Fast Switching Time, in: Microelectronics, Circuits and Systems, Springer, 2021, pp. 213-223.

[15] M. Pashapour, S.-M. Pesteii, G. Rezazadeh, S. Kouravand, Thermo-Mechanical Behavior of a Bilayer Microbeam Subjected to Nonlinear Electrostatic Pressure, Sensors & Transducers, 103(4) (2009) 161.

[16] W.-M. Zhang, H. Yan, Z.-K. Peng, G. Meng, Electrostatic pull-in instability in MEMS/NEMS: A review, Sensors and Actuators A: Physical, 214 (2014) 187-218.

[17] H.M. Ouakad, N. Alcheikh, S.B. Mbarek, R. Rocha, M.I. Younis, Statics and Dynamics of V-Shaped Microbeams Under Axial Forces, Journal of Computational and Nonlinear Dynamics, 16(9) (2021) 34-50.

[18] H.M. Sedighi, F. Daneshmand, J. Zare, The influence of dispersion forces on the dynamic pull-in behavior of vibrating nano-cantilever based NEMS including fringing field effect ,Archives of Civil and Mechanical Engineering, 14(4) (2014) 766-775.

[19] Nozim N. Khoshimov, Alisher A. Mukhtorov, Kabil E. Nasirov, Rakhmatilla N. Rakhimov, Rahmatjon R. Mamadaminov. Effects of Polyphenols on changes in the transport of Ca2+ NMDA-receptors under the influence of L-glutamate. Research Journal of Pharmacy and Technology 2023; 16(3):1205-3. doi: 10.52711/0974-360X.2023.00200.

[20] D. Kalafut, A. Bajaj, A. Raman, Multistability of cantilever MEMS/NEMS switches induced by electrostatic and surface forces, International Journal of Non-Linear Mechanics, 95 (2017) 209-215.

[21] H. Haghshenas Gorgani, M. Mahdavi Adeli, M. Hosseini, Pull-in behavior of functionally graded micro/nano-beams for MEMS and NEMS switches, Microsystem Technologies, 25(8) (2019) 3165-3173.

[22] E. Taati, N. Sina, Static Pull-in Analysis of Electrostatically Actuated Functionally Graded Micro-Beams Based on the Modified Strain Gradient Theory, International Journal of Applied Mechanics, 10(03) (2018) 23-41.

[23] S. Kong, A Review on the Size-Dependent Models of Micro-beam and Micro-plate Based on the Modified Couple Stress Theory, Archives of Computational Methods in Engineering, 29(1) (2022) 1-31.

[24] R. Kumar, Materials Selection Approaches and Fabrication Methods in RF MEMS Switches, Journal of Electronic Materials, 45 (2021) 1-20.

[25] Aswathanarayan M.S., Reddappa H.N. (2024), Exploring the Tribological Response of Graphene Reinforce Glass – Epoxy Nano Composites: Effect of Process Parameters , Journal of Materials and Engineering, 2(3), 186-194, 10.61552/JME.2024.03.004.

[26] Mamyrbayev, O., Akhmediyarova, A., Oralbekova, D., Alimkulova, J., & Alibiyeva, Z. (2025). Optimizing Renewable Energy Integration Using IoT and Machine Learning Algorithms. International Journal of Industrial Engineering and Management, 16(1), 101–112. https://doi.org/10.24867/IJIEM-375

[27] A. Farzaneh, M.D. Esrafili, Ö. Mermer, Development of TiO2 nanofibers based semiconducting humidity sensor: adsorption kinetics and DFT computations, Materials Chemistry and Physics, 239 (2020) 121981.

[28] Medojević, M., & Medojević, M. (2017). Simulation Based Productivity Forecast of 1 MW PV Power Plant in the Weather Conditions Typical for Belgrade Region. International Journal of Industrial Engineering and Management, 8(2), 91–97. https://doi.org/10.24867/IJIEM-2017-2-110.

[29] Mahmoodi-k, M., Davoodabadi, I., Višnjić, V., & Afkar, A. (2014). Stress and dynamic analysis of optimized trailer chassis. Tehnički vjesnik, 21(3), 599-608.

[30] Khayitov, O., Saidova, L., Galiev, S., Umirzokov, A., & Mahkamov, M. (2023). Interrelation of performance indicators of technological transport with mining conditions of a quarry. NEWS of National Academy of Sciences of the Republic of Kazakhstan, 226-239.

[31] F. Bourada, A.A .Bousahla, A. Tounsi, E. Bedia, S. Mahmoud, K.H. Benrahou, A. Tounsi, Stability and dynamic analyses of SW-CNT reinforced concrete beam resting on elastic-foundation, Computers and Concrete, 25(6) (2020) 485-495.

[32] M. Asghari, M. Kahrobaiyan, M. Nikfar, M .Ahmadian, A size-dependent nonlinear Timoshenko microbeam model based on the strain gradient theory, Acta Mechanica, 223(6) (2012) 1233-1249.

[33] M. Şimşek, T. Kocatürk, Nonlinear dynamic analysis of an eccentrically prestressed damped beam under a concentrated moving harmonic load, Journal of Sound and Vibration, 320(1-2) (2009) 235-253.

[34] H. Liu, S. Shen, K. Oslub, M. Habibi, H. Safarpour, Amplitude motion and frequency simulation of a composite viscoelastic microsystem within modified couple stress elasticity, Engineering with Computers, **56**, (2021) 1-15.

[35] A. Noghrehabadi, M. Ghalambaz, A. Ghanbarzadeh, A new approach to the electrostatic pull-in instability of nanocantilever actuators using the ADM–Padé technique, Computers & Mathematics with Applications, 64(9) (2009) 48-59.

[36] J. Abdi, A. Koochi, A.S. Kazemi, M. Abadyan, Modeling the effects of size dependence and dispersion forces on the pull-in instability of electrostatic cantilever NEMS using modified couple stress theory, Smart Materials and Structures, 20(5) (2011) 34-41.

[37] Paykani, A., Khosravi, M., Saeimi-Sadigh, M. A., & Mahmoodi-Kaleibar, M. (2013). Dynamic analysis and design of V-shape plates under blast loading. Journal of Vibroengineering, 15(2), 971-978.

[38] L.-L. Ke, J. Yang, S. Kitipornchai ,An analytical study on the nonlinear vibration of functionally graded beams, Meccanica, 45(6) (2010) 743-752.

[39] P. Goel, K. Vinoy, A low cost approach for the fabrication of microwave phase shifter on laminates, Microsystem technologies, 17(10) (2011) 1653-1660.

[40] H. Hu, L. Reven, A. Rey, First-principles density functional theory (DFT) study of gold nanorod and its interaction with alkanethiol ligands, The journal of physical chemistry. B, 117 41 (2013) 12625-12631.